Nonaqueous-phase-liquid dissolution in variable-aperture fractures: Development of a depth-averaged computational model with comparison to a physical experiment

Russell L. Detwiler[1] and Harihar Rajaram

Department of Civil, Environmental, and Architectural Engineering, University of Colorado
Boulder, Colorado, USA

Robert J. Glass

Flow Visualization and Processes Laboratory, Sandia National Laboratories, Albuquerque, New Mexico, USA

Abstract. Dissolution of nonaqueous-phase liquids (NAPLs) from variable-aperture fractures couples fluid flow, transport of the dissolved NAPL, interphase mass transfer, and the corresponding NAPL-water-interface movement. Each of these fundamental processes is controlled by fracture-aperture variability and entrapped-NAPL geometry. We develop a depth-averaged computational model of dissolution that incorporates the fundamental processes that control dissolution at spatial resolutions that include all scales of variability within the flow field. Thus this model does not require empirical descriptions of local mass transfer rates. Furthermore, the depth-averaged approach allows us to simulate dissolution at scales that are larger than the scale of the largest entrapped NAPL blobs. We compare simulation results with an experiment in which we dissolved residual entrapped trichloroethylene (TCE) from a 15.4 × 30.3 cm, analog, variable-aperture fracture. We measured both fracture aperture and the TCE distribution within the fracture at high spatial resolution using light transmission techniques. Digital images acquired over the duration of the experiment recorded the evolution of the TCE distribution within the fracture and are directly compared with the results of a computational simulation. The evolution with time of the distribution of the entrapped TCE and the total TCE saturation are both predicted well by the dissolution model. These results suggest that detailed parametric studies, employing the depth-averaged dissolution model, can be used to develop a comprehensive understanding of NAPL dissolution in terms of parameters characterizing aperture variability, phase structure, and hydrodynamic conditions.

1. Introduction

Nonaqueous-phase liquids (NAPLs) released to the subsurface can dissolve into groundwater, creating a potential long-term contamination source. Predicting the magnitude and duration of contamination caused by an entrapped NAPL source requires locating and quantifying the source and subsequently understanding the mechanisms that control dissolution rates. Predicting NAPL dissolution rates in porous and fractured media requires a fundamental understanding of the morphology of the entrapped NAPL, fluid flow and dissolved NAPL transport around blobs of entrapped NAPL, and mass transfer across NAPL-water interfaces. A number of researchers have studied NAPL dissolution in porous media using column-scale experiments. These studies typically result in empirical expressions that relate a mass transfer coefficient (representing the rate of NAPL dissolution at the scale of the experiment) to variables such as the Peclet number (Pe = advective/diffusive

transport) and the NAPL saturation (S_N) [e.g., *Miller et al.*, 1990; *Powers et al.*, 1992; *Imhoff et al.*, 1994; *Powers et al.*, 1994]. Such efforts have led to significant insights into the factors controlling dissolution in the specific experimental systems and demonstrate the influence of relevant parameters, such as Pe and S_N, on the empirical expressions. However, because these expressions cannot incorporate the details of the pore geometry and entrapped-NAPL structure, they do not lead to general relationships applicable over a wide range of porous medium properties.

Development of a general understanding of the dynamics of NAPL dissolution requires pore-scale investigations that explicitly include the role of pore geometry and entrapped-NAPL structure on small-scale hydrodynamics (i.e., flow, mass transport, and mass transfer). Such approaches may lead to a framework for predicting dissolution rates in arbitrary porous media, as a function of porous medium geometry and hydrodynamic processes. *Kennedy and Lennox* [1997], *Jia et al.* [1999], and *Dillard and Blunt* [2000] have recently reported such investigations. In a porous medium consisting of a single layer of glass beads, *Kennedy and Lennox* [1997] measured the dissolution of individual NAPL blobs in the form of spheres and pendular rings. They inferred mass transfer coefficients for individual NAPL blobs, assuming zero concentrations in the surrounding water and local equilibrium dissolution at the

water-NAPL interface. They hypothesized that variability in the measured dissolution rates for individual NAPL blobs was due to variability in the pore velocities around each blob caused by differing pore geometries. *Jia et al.* [1999] conducted dissolution experiments in a two-dimensional pore network etched in glass and measured the concentration of dissolved NAPL in the outflow from their experiment. This approach allowed them to directly observe the geometry of NAPL blobs over the entire network. Pore-network dissolution simulations, based on experimentally measured phase distributions, demonstrated the need to incorporate the influence of advection on local mass transfer rates. By using an empirical expression to calculate local mass transfer coefficients, they obtained good agreement between simulations and experiments. *Dillard and Blunt* [2000] developed a three-dimensional pore-network model of NAPL dissolution and compared their model predictions with the experimental results of *Powers et al.* [1992]. To obtain reasonable agreement between the experimental results and simulations, they coupled a local equilibrium condition at the NAPL-water interfaces with a simplified conceptual model of diffusion into a corner [*Zhou et al.*, 2000] to model mass transfer into the flowing water. The results of these previous studies highlight the importance of either accurately simulating the velocity near the NAPL-water interfaces or choosing an appropriate empirical or conceptual model of local interphase mass transfer.

NAPL migration into fractured media has been reported [e.g., *Schwartz et al.*, 1982; *Mackay and Cherry*, 1989]; however, relatively few studies have focused on the physical processes controlling NAPL dissolution in fractures. As in porous media, NAPL dissolution in fractures will be controlled by flow and transport around the entrapped NAPL, which is directly related to the entrapped phase structure and pore geometry (or fracture aperture). Entrapped-NAPL blobs in fractures can exhibit a wider range of size and complexity than in porous media. Several researchers have demonstrated that for well-sorted sands, NAPL blobs are mostly "singlets" (i.e., they occupy a single pore body) [e.g., *Larson et al.*, 1981; *Conrad et al.*, 1992]. Subsequent investigations observed that the range of NAPL blob sizes increases with grain-size variability [*Mayer and Miller*, 1992; *Powers et al.*, 1992] and Bond number ($Bn =$ buoyancy/capillary forces) [*Mayer and Miller*, 1992]. In fractures, Bn depends not only on the difference in densities between NAPL and water, but also on the orientation of the fracture plane. Thus, for a single NAPL-water pair, a wide range of entrapped phase structures is possible depending on the fracture orientation. In a horizontal fracture (i.e., $Bn = 0$), typical "lengths" of blobs may be 2–3 orders of magnitude larger than the correlation scale (λ) of the aperture field [e.g., *Glass et al.*, 1998, 2000]. *Glass and Nicholl* [1995] observed that during dissolution, locations of fast interface movement do not necessarily coincide with locations of high mass transfer rates. The implication is that blob shrinkage is controlled by capillary forces. *Glass et al.* [1998, 2000] demonstrated that the interface movements resulting from dissolution of a single blob of nonaqueous phase could be simulated using a modified invasion percolation (MIP) algorithm. Thus, to effectively simulate the shrinkage of an individual NAPL blob, dissolution models should couple mass transfer, across the entire NAPL-water interface, to capillary physics along the interface. Such a coupling has not been represented in previous pore-scale dissolution models.

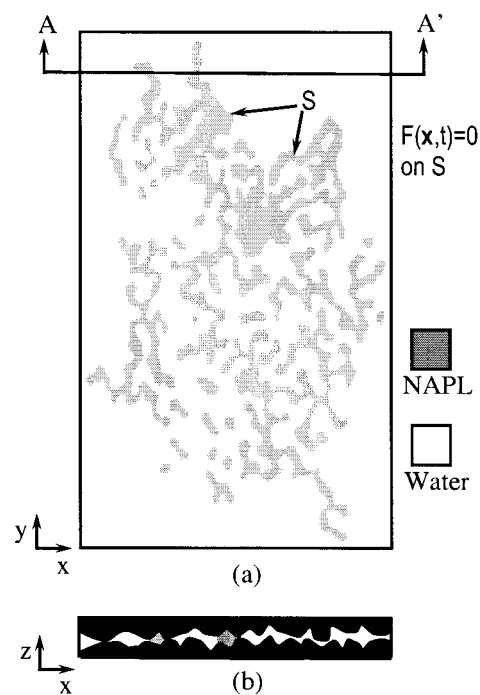In this paper we present a computational model of en-

Figure 1. (a) Plan view and (b) cross section of the three-dimensional flow field in a variable-aperture fracture containing regions of entrapped nonaqueous-phase liquid (NAPL).

trapped NAPL dissolution in variable-aperture fractures that explicitly incorporates the small-scale geometry of individual NAPL blobs. The model couples depth-averaged models of flow, dissolved-NAPL transport, and interphase mass transfer to determine mass transfer rates from each individual NAPL blob. The resulting interface movement is calculated using the MIP algorithm [*Glass et al.*, 1998, 2000]. A direct comparison of a computational simulation to a physical experiment demonstrated that the simulation predicted both the fracture-scale mass transfer rate and the evolution of NAPL distribution within the fracture very well. This is especially encouraging because the computational model explicitly incorporates the fundamental processes controlling dissolution and thus does not rely on empirical parameters to describe the interphase mass transfer process. These positive results suggest that the depth-averaged approach can be used effectively to develop a comprehensive understanding of the role of different parameters, such as phase structure, aperture variability, and Pe, on NAPL dissolution from variable-aperture fractures.

2. Model Development

The process of depth averaging the three-dimensional equations governing flow and transport in a variable-aperture fracture requires simplifying assumptions. To understand the implications of depth averaging for modeling dissolution, it is instructive to first consider the three-dimensional description of dissolution. Figure 1, a schematic of the flow field in a variable-aperture fracture occupied by residual entrapped NAPL, shows the three-dimensional void space in the fracture. A fully descriptive mathematical model of the dissolution of the entrapped NAPL from this void space will effectively couple fluid flow, mass transport through the flowing phase, mass transfer from the entrapped phase into the flowing phase, and

interface movement induced by the shrinking entrapped phase. Note that we assume that the solubility of water in NAPL is negligible. In some fracture systems, interaction with the rock matrix will also play a significant role in NAPL dissolution; however, we limit this investigation to fractures in an impermeable, nonporous rock matrix.

This section summarizes the three-dimensional equations describing fluid flow (section 2.1), mass transport (section 2.2), and mass transfer and interface movement (section 2.3), followed by presentation of a scaling argument for reducing these equations to quasi steady state equations (section 2.4) and a discussion of the implications of depth averaging (section 2.5).

2.1. Fluid Flow

Slow (i.e., low Reynolds number), three-dimensional, unsteady fluid flow through a variable-aperture fracture is described by the Stokes equations:

$$\frac{\partial \mathbf{u}}{\partial t} = -\nabla p + \mu \nabla^2 \mathbf{u} \tag{1a}$$

$$\frac{\partial \hat{\mathbf{u}}}{\partial t} = -\nabla \hat{p} + \hat{\mu} \nabla^2 \hat{\mathbf{u}} \tag{1b}$$

$$\nabla \cdot \mathbf{u} = 0 \tag{2a}$$

$$\nabla \cdot \hat{\mathbf{u}} = 0, \tag{2b}$$

where (1a) and (2a) describe flow in the water and (1b) and (2b) describe flow within the entrapped-NAPL blobs. In (1a) and (2a), $\mathbf{u}$, p, and μ are the velocity vector, the dynamic pressure, and the viscosity, respectively; in (1b) and (2b) the corresponding variables for the NAPL are denoted by a circumflex. Assumptions inherent in this representation of the Stokes equations are that both fluids are incompressible with constant viscosities. The time-derivative terms in (1a) and (1b) result from interface movement as the NAPL blobs dissolve. Equations (1) and (2) describe flow both in the freely flowing aqueous phase and inside the entrapped nonaqueous phase; momentum transfer across the interface drives flow in the entrapped phase. The location of the NAPL-water interfaces ($S_m(t)$, where m denotes the mth blob) at any time t, are described by some function $F_m(\mathbf{x}, t)$ such that $F_m(\mathbf{x}, t) = 0$ on $S_m(t)$ (Figure 1). Solving (1) and (2) requires the following boundary conditions on the NAPL-water interfaces [e.g., *Leal*, 1992, pp. 199–205]:

Continuity of velocity

$$\mathbf{u} = \hat{\mathbf{u}} \text{ on } S_m(t). \tag{3}$$

Kinematic condition on the interface

$$\frac{DF_m(\mathbf{x}, t)}{Dt} = \frac{1}{|\nabla F_m|} \frac{\partial F_m}{\partial t} + \mathbf{u} \cdot \mathbf{n} = \frac{1}{|\nabla F_m|} \frac{\partial F_m}{\partial t} + \hat{\mathbf{u}} \cdot \mathbf{n}$$

$$= 0 \text{ on } S_m(t), \tag{4}$$

where $\mathbf{n}$ is the unit vector normal to the NAPL-water interface. This condition requires that in both fluids, the component of the fluid velocity normal to the interface is equal to the corresponding velocity of the interface.

Dynamic stress conditions at the interface, including the normal stress balance

$$(\hat{p} - p) + [((\boldsymbol{\tau} - \hat{\boldsymbol{\tau}}) \cdot \mathbf{n}) \cdot \mathbf{n}] - \sigma(\nabla \cdot \mathbf{n}) = 0 \text{ on } S_m(t). \tag{5}$$

Tangential stress balance

$$((\boldsymbol{\tau} - \hat{\boldsymbol{\tau}}) \cdot \mathbf{n}) \cdot \mathbf{t}_l + (\nabla \sigma) \cdot \mathbf{t}_l = 0 \text{ on } S_m(t), \tag{6}$$

where $\boldsymbol{\tau}$ is the shear stress tensor in each fluid at the interface, $\mathbf{t}_l$ ($l = 1, 2$) are two orthogonal unit tangent vectors that are normal to $\mathbf{n}$, and σ is the interfacial tension. The second term in (5) is the sum of the normal components of the differential stress tensor. In the absence of fluid velocity (or for very low fluid velocities, i.e., $\boldsymbol{\tau} = \hat{\boldsymbol{\tau}} \cong 0$), equation (5) becomes the Young-Laplace equation, which relates capillary pressure to the interfacial tension and interfacial curvature ($\nabla \cdot \mathbf{n}$). If σ is constant along the interface, the second term in (6) reduces to zero and (6) requires that the tangential components of the shear stress tensors on either side of the interface must be equal. Variations in σ over the interface can result when molecules adsorb to an interface at varying concentrations. This can induce fluid flows near the interface that are commonly referred to as Marangoni convection [e.g., *Leal*, 1992]. In cases of extreme σ gradients along NAPL-water interfaces, such as during surfactant enhanced mobilization, the large reduction in σ at the upstream end of each NAPL blob can cause blobs to mobilize in the direction opposite to the mean flow direction [*Zhong et al.*, 2001] (hereinafter referred to as ZMG).

Boundary conditions for the fluid flow equations must also be specified on the domain boundaries. These are the no-slip condition ($\mathbf{u} = 0$ and $\hat{\mathbf{u}} = 0$) on the two fracture surfaces and some problem-specific boundary conditions surrounding the domain in the fracture plane.

2.2. Mass Transport

Three-dimensional, unsteady transport of the dissolved component of NAPL in the flowing water is described by the familiar advection-diffusion equation:

$$\frac{\partial c}{\partial t} + \nabla \cdot (\mathbf{u}c) = \nabla \cdot (D_M \cdot \nabla c), \tag{7}$$

where D_M is the molecular diffusion coefficient of NAPL dissolved in water (assumed scalar) and c is the local aqueous-phase mass concentration of NAPL in water. The dissolved NAPL concentration at the NAPL-water interfaces is assumed to be at the solubility limit (c_s), resulting in constant concentration boundary conditions along each NAPL-water interface:

$$c = c_s \text{ on } S_m(t). \tag{8}$$

In addition to (8), problem-specific boundary conditions must be applied at the domain boundaries, including the upstream concentration of dissolved NAPL, c_o. Because we are assuming a single-component NAPL and neglecting dissolution of water in the NAPL, there is no need to describe transport within the entrapped NAPL.

2.3. Mass Transfer and Interface Movement

The boundary condition specified by (8) results in local mass flux (j) described by

$$j = D_M \nabla c \cdot \mathbf{n} \text{ on } S_m(t). \tag{9}$$

The total rate of mass transfer from the mth NAPL blob (J_m) at any time is then given by

$$J_m = \int_{S_m} j \, da = \rho \frac{d}{dt}(V_m), \tag{10}$$

where da is an elemental area of the interfacial surface (S_m), ρ is the density of the entrapped NAPL, and V_m is the volume of the blob. As the volume of the blob decreases, the interface between the two fluids must recede while satisfying (3), (4), (5), and (6).

The NAPL-water interface moves as mass is transferred from each NAPL blob to the flowing aqueous phase and must satisfy (5). If viscous forces are negligible compared with capillary forces, interface movement is completely controlled by capillary forces. It is reasonable to expect that the ratio of viscous forces to capillary forces (the capillary number, Ca) will be small in fractures with slow flow velocities and small apertures [e.g., *Glass et al.*, 1998, 2000]. Thus (5) simplifies to

$$P_c = -\sigma(\nabla \cdot \mathbf{n}), \tag{11}$$

where $P_c = p - \hat{p}$ is the local capillary pressure and $\nabla \cdot \mathbf{n}$ represents the interfacial curvature.

2.4. Quasi Steady State Approximation

An intuitive expectation that the changes in geometry associated with dissolving NAPL blobs are much slower than the rates of transport of the dissolved NAPL in the aqueous phase motivates the development of a quasi steady state approximation for flow and transport. In this section we present a rigorous derivation of the quasi steady state approximation following the procedure of *Ortoleva et al.* [1987]. The critical step in this derivation is the introduction of a small parameter $\varepsilon = (c_s - c_o)/\rho$, which, for trichloroethylene (TCE) dissolving into clean water ($c_o = 0$, $c_s = 1280$ mg/L, and $\rho = 1.465$ g/cm^3), has a value of 8.7×10^{-4}. It is evident from (10) that the rate of change of volume of an individual blob, J_m/ρ, scales as $(c_s - c_o)/\rho$, because J_m will scale with $(c_s - c_o)$. This, and the expectation that blob volumes change relatively slowly, prompts the introduction of a new time variable:

$$T = \varepsilon t. \tag{12}$$

Changes in the entrapped-phase geometry occur at timescales of order t, and changes in the pressure and concentration fields occur at timescales of order T. Equations (1), (4), (7), and (10) can be rewritten in terms of T and the dimensionless concentration, $\phi = (c - c_o)/(c_s - c_o)$:

$$\varepsilon \frac{\partial \mathbf{u}}{\partial T} = -\nabla p + \mu \nabla^2 \mathbf{u} \tag{13}$$

$$\frac{\varepsilon}{|\nabla F|} \frac{\partial F}{\partial T} + \mathbf{u} \cdot \mathbf{n} = 0 \tag{14}$$

$$\varepsilon \frac{\partial \phi}{\partial T} + \nabla \cdot (\mathbf{u} \phi) = D_m \nabla^2 \phi \tag{15}$$

$$\varepsilon \frac{d}{dT}(V_m) = \int_S D_M \nabla \phi \cdot \mathbf{n} \, da. \tag{16}$$

If we now consider $\varepsilon \to 0$, both flow and transport can be represented by a sequence of quasi steady state solutions corresponding to the current entrapped-phase geometry. Additionally, for each quasi steady state time step, the kinematic interface condition (14) reduces to a condition of zero normal velocity at the NAPL-water interface. Equations analogous to (13) and (14) can be written for the NAPL also. However, as discussed previously, because we have assumed that the solubility of water in NAPL is negligible and that the NAPL consists of a single component, there is no need to solve for flow and transport within the NAPL blobs.

2.5. Depth-Averaged Equations

The equations discussed in the previous sections fully describe flow, transport, and dissolution in the two-phase system shown in Figure 1. To allow numerical implementation of these equations at reasonably large scales (10^6–10^7 grid points), we depth average the three-dimensional equations, resulting in a set of two-dimensional equations that retain the coupling between flow, transport, interfacial mass transfer, and interface movement. Depth-averaged models have been used widely for both flow [e.g., *Tsang and Witherspoon*, 1981; *Brown*, 1987; *Gelhar*, 1987] and transport [e.g., *Gelhar*, 1987; *Moreno et al.*, 1988; *Thompson*, 1991] through variable-aperture fractures. In this section we describe the two-dimensional governing equations that result from depth averaging and discuss the implications of the implicit assumptions.

Averaging the three-dimensional quasi steady Stokes equations (2a) and (13) across the fracture aperture results in $\nabla \cdot (b\mathbf{v}) = 0$, where the depth-averaged velocity, $\mathbf{v} = b^2 g/12\nu \nabla h$, which when combined yield the well-known, two-dimensional Reynolds equation:

$$\nabla \cdot \left(\frac{b^3 g}{12 \nu} \nabla h \right) = 0, \tag{17}$$

where $h = p/(\rho g)$ is the local pressure head in a horizontal fracture and b is the local aperture. The assumptions required in developing (17) are that pressure is constant across the fracture aperture (i.e., $\partial p/\partial z = 0$) and that the aperture varies slowly in space. These conditions are met if $\langle b \rangle/\lambda$ and $\sigma_b/\langle b \rangle$ are small, where $\langle b \rangle$ is the mean fracture aperture and λ and σ_b are the correlation length and standard deviation of aperture variability, respectively [e.g., *Zimmerman and Bodvarsson*, 1996; *Nicholl et al.*, 1999]. Note that h is a potential function for velocity so that (17) essentially represents a two-dimensional inviscid flow, and for the flow geometry shown in Figure 1, the only boundary condition that can be meaningfully imposed on the flowing phase at the fluid-fluid interfaces is

$$\nabla h \cdot \mathbf{n} = 0. \tag{18}$$

Thus, in addition to reducing the computational expense of calculating the flow field, the simplification to two dimensions precludes incorporating momentum transfer across the NAPL-water interfaces as described by (5) and (6).

Recent comparisons of flow experiments in measured aperture fields with numerical simulations based on the Reynolds equation indicate that the Reynolds equation overestimates flow in some variable-aperture fractures [*Yeo et al.*, 1998; *Nicholl et al.*, 1999]. However, *Adler and Thovert* [1999] suggest that these discrepancies may be small in many natural fractures. Similar comparisons in partially saturated fractures [*Nicholl et al.*, 2000] have demonstrated good agreement between experimentally measured and simulated relative permeabilities (k_{rw} = partially saturated permeability/saturated permeability). This indicates that an entrapped nonaqueous phase does not contribute significantly to errors in fracture-scale flow estimates.
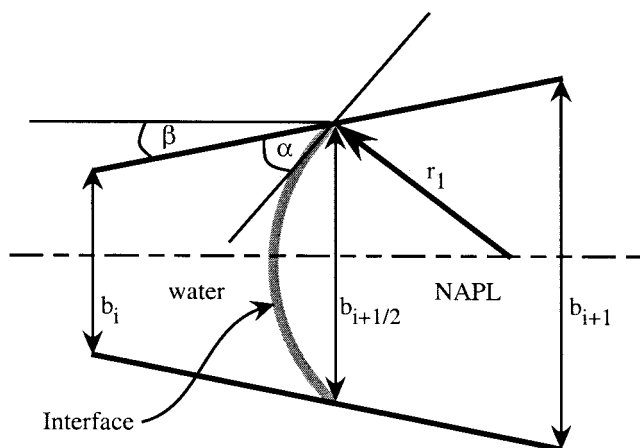
Figure 2. Schematic demonstrating critical angles for calculating local corrections to interfacial area due to curvature (with radius r_1) across the fracture aperture. Here α is the contact angle and β is the convergence/divergence angle of the fracture surfaces. The curvature described by r_1 influences both the interfacial area and the local capillary pressures. The actual interfacial length across the aperture is equal to $\xi_1 b_{i+1/2}$.

Depth averaging (15) results in the quasi steady, two-dimensional equation for mass transport through a variable-aperture fracture:

$$\nabla \cdot (b\mathbf{v}C) = \nabla \cdot (b\mathbf{D}_{eff} \cdot \nabla C), \qquad (19)$$

where $\mathbf{D}_{eff}$ is the effective dispersion tensor, C represents the average of the three-dimensional concentration (c) across the fracture aperture, and the depth-averaged boundary condition on the NAPL-water interfaces is $C = C_s$. In general, $\mathbf{D}_{eff}$ will be different from D_m due to depth averaging (15). Velocity profiles across the fracture aperture cause increased dispersion in the flow direction (Taylor dispersion), which must be captured by an effective dispersion coefficient.

Though we are solving a two-dimensional approximation to the governing equations, it is critical that the curvature of the interface across the aperture be included in the formulation of (11) because it may contribute more to the pressure drop across the interface than the in-plane curvature. In a fracture, $\nabla \cdot \mathbf{n}$ can be quantified in terms of the two principal radii of curvature, r_1 and r_2, as $1/r_1 + 1/r_2$, where r_1 is the radius of curvature across the aperture and r_2 is the radius of curvature in the plane of the fracture (Figures 2 and 3). *Glass et al.* [1998, 2000] demonstrated that an MIP algorithm that includes both r_1 and r_2 describes the interface recession during dissolution of an individual blob. However, it must be coupled with the previously described flow, transport, and mass transfer algorithms to estimate the dissolution rate for individual blobs and simultaneously model the dissolution of multiple blobs.

3. Computational Algorithm

Our depth-averaged computational model of NAPL dissolution is based on coupling the two-dimensional equations for flow, transport, and mass transfer with the MIP algorithm for modeling interface movement. In this section we describe the details of the computational dissolution algorithm, which consists of the following steps:
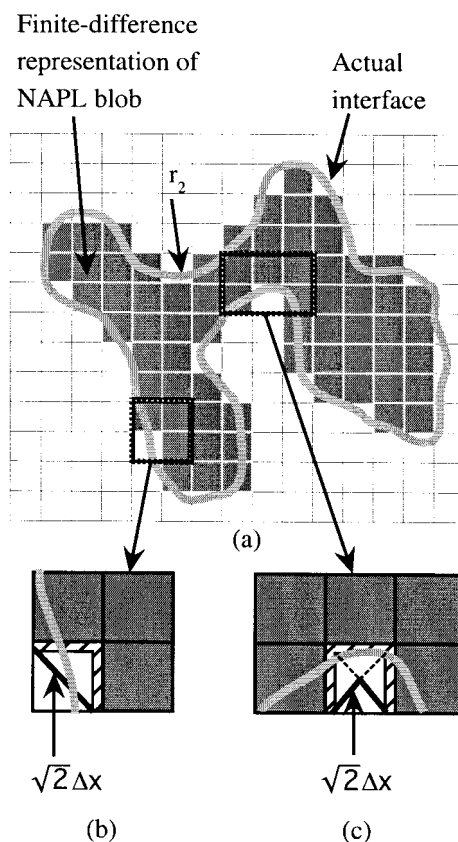

Figure 3. Schematic demonstrating the in-plane radius of curvature (r_2) and corrections to interfacial area (Figure 3a) due to misrepresentation of the curved interfaces by the finite difference discretization. For interface geometries conforming to Figure 3b or 3c, the length of the highlighted grid-block faces are multiplied by $\xi_2 = \sqrt{2}/2$ or $\sqrt{2}/3$, respectively.

1. Locate each discrete NAPL blob and identify each with a unique integer.

2. Solve for the quasi steady state pressure field for the given phase distribution using the Reynolds equation (17) with the appropriate boundary conditions (18).

3. Calculate local velocities using the pressure and aperture fields and solve for the quasi steady concentration field using the depth-averaged transport equation (19) with equilibrium boundary conditions ($C = C_s$) on NAPL-water interfaces.

4. Calculate mass transfer rates from each discrete NAPL blob by numerically integrating local mass transfer rates around the perimeter of each blob.

5. Calculate the amount of mass removed from each blob during the current time step.

6. Change the phase state (i.e., from NAPL to water) of individual grid blocks in each blob in the order specified by the MIP algorithm until the appropriate mass is removed for the current time step.

7. Return to step 1 and iterate until all NAPL is removed from the fracture.

The computational model numerically approximates the flow field using a centered finite difference approximation of (17) and solves the resulting system of equations using an efficient algebraic multigrid algorithm (AMG) developed by *Ruge and Stüben* [1987]. To solve for C in the fracture during

each time step, the model discretizes (19) using an upstream-difference approximation to the advective term and a centered-difference approximation to the diffusive term and solves the resulting system of equations using the AMG algorithm. Note that in locations with steep concentration gradients and high flow velocities (i.e., near NAPL-water interfaces), this discretization scheme results in numerical dispersion in the local flow direction. Because the numerical dispersion coefficient is proportional to $\mathbf{v}\Delta x$, we use a grid-refinement study to evaluate the influence of numerical dispersion on dissolution simulations in section 5.

As discussed in section 2.5, implementation of (19) requires a depth-averaged dispersion tensor, $\mathbf{D}_{\mathrm{eff}}$. For fully developed Taylor dispersion in Poiseuille flow between parallel plates, $\mathbf{D}_{\mathrm{eff}} = D_m + \mathbf{V}^2 b^2/210 D_m$, where $\mathbf{V}$ is the depth-averaged velocity vector. *Detwiler et al.* [2000] showed that the effective Taylor dispersion coefficient at large solute displacements in a variable-aperture fracture has a similar form, with $\mathbf{V}$ replaced by the mean solute velocity and b replaced by the mean aperture. However, depending on the scale of the grid blocks used to discretize the flow domain, Taylor dispersion may not become fully developed within individual grid blocks, and thus the appropriate value for $\mathbf{D}_{\mathrm{eff}}$ will fall between D_m and $D_m(1 + Pe^2/210)$, where $Pe = \mathbf{V}b/D_m$ (based on local grid block values of $\mathbf{V}$ and b). We investigate the sensitivity of mass transfer rates to the value of $\mathbf{D}_{\mathrm{eff}}$ by simulating dissolution using these two extreme estimates of $\mathbf{D}_{\mathrm{eff}}$ in section 5.

For each quasi steady state time step, the code performs AMG cycles on the matrices resulting from the discretization of the flow and transport equations until the 2-norm of the residual vector falls below a problem-specific small value. Convergence of the solver is then checked by calculating flux balance errors for water and NAPL. Water flux balance error is calculated as (inflow − outflow)/outflow, and the NAPL flux balance error is calculated as (mass flux at outflow − total mass flux from all NAPL blobs)/(mass flux at outflow). For the simulation discussed in detail in section 5, the flux balance errors were less than 8.3×10^{-10} and 1.2×10^{-7} for water and NAPL, respectively, indicating excellent mass conservation.

By specifying a constant concentration boundary condition ($C = C_s$) along each NAPL-water interface, we simulate local equilibrium mass transfer. After solving the quasi steady state transport equation (19) over the domain, the mass transfer rate from each NAPL blob must be calculated. The model calculates the mass flux across each grid-block face that lies on a NAPL-water interface using the discrete expression corresponding to (9):

$$j_{\mathrm{int}} = AD_M(C_s - C_i)/(\Delta x/2), \qquad (20)$$

where j_{int} is the mass flux across the local interface with area A, C_s is the equilibrium concentration assigned to the interface, C_i is the computed concentration of the cell adjacent to the interface, and $\Delta x/2$ is the distance between the center of cell i and the interface. The total rate of mass transfer from each NAPL blob is calculated by numerically integrating j_{int} over the entire interfacial area.

Using (20) to describe mass flux across NAPL-water interfaces requires estimating the interfacial area, A. We estimate A as

$$A = \xi \Delta x b_{i+1/2}, \qquad (21)$$

where $b_{i+1/2}$ is the mean of the grid-block apertures on either side of the interface and ξ is a correction factor that accounts

for local interfacial curvature. Here ξ is the product of ξ_1, a correction factor for underestimation of the interface length across the aperture (Figure 2), and ξ_2, a correction factor for overestimation of the interface length in the fracture plane (Figure 3).

Using the geometry described by Figure 2, ξ_1 is given by

$$\xi_1 = \frac{\pi/2 - \alpha - \beta}{\cos(\alpha + \beta)}, \qquad (22)$$

where

$$\beta = \tan^{-1}\left(\frac{b_{i+1} - b_i}{2\Delta x}\right). \qquad (23)$$

In (22), α is the water-NAPL-solid contact angle and β is the angle of the fracture surface with respect to the fracture center plane. The angle β, given by (23), is a well-defined function of the aperture field. As long as the NAPL is the nonwetting fluid, β will always be positive. Thus the limiting range of ξ_1 is from 1 ($\alpha = \pi/2$ and $\beta = 0$, resulting in a flat interface) to $\pi/2$ ($\alpha = 0$ and $\beta = 0$, resulting in a semicircular interface). For other system-specific values of α and β, ξ_1 will modify the interfacial length by a factor between 1 and $\pi/2$.

Imposing the finite difference grid onto the curved NAPL-water interfaces results in overestimations of the local interfacial length in the fracture plane. We define the correction factor for curvature in the fracture plane, ξ_2, by assuming that the actual interface is more closely approximated by the geometry shown in Figure 3b and 3c. On the basis of this geometry, ξ_2 reduces the length of each of the highlighted interfaces in Figures 3b and 3c by a factor of $\sqrt{2}/2$ and $\sqrt{2}/3$, respectively.

The MIP algorithm calculates the global order in which NAPL-filled grid blocks are replaced by water as each blob dissolves. For each MIP iteration, P_c is calculated for each NAPL-filled grid block lying on an interface. The TCE-water-glass contact angle α is used, along with the local aperture, to calculate r_1, and λ is used to determine a grid-independent length of interface that is included in local calculations of r_2. The values of P_c over the entire field are sorted, and the cell with the lowest value is replaced by water. This process is repeated until all NAPL has been replaced by water (for full MIP implementation details, see *Glass et al.* [1998, 2000]). The MIP algorithm yields a field in which each initially NAPL-filled cell is labeled with a unique integer that corresponds to the order in which it becomes water-filled. Coupling this global dissolution order with local mass transfer rates requires identifying each discrete NAPL blob and converting the values corresponding to the global dissolution order to a local order for each individual blob. This process is repeated at the beginning of each time step to properly account for blobs that have split in the previous time step.

In each time step, for each NAPL blob, the dissolution algorithm removes an amount of mass equal to the local mass transfer rate multiplied by the time step duration. Individual cells are filled corresponding to the local invasion order until the required mass has been removed. Typically, the final grid block to be filled will contain more mass than is needed to complete the time step, and thus the mass of NAPL in that grid block is reduced, and it is the first grid block to be filled with water during the next time step. Each flow and transport simulation considers partially dissolved grid blocks to be NAPL-filled. Results of simulations using different values of Δt (discussed in section 5) suggest that this simplification has a negligible influence on the results of dissolution simulations.

Table 1. Fracture Dimensions and Measured Aperture Statistics

Parameter	Value
Dimensions, cm	15.4×30.3
Dimensions, pixels	995×1952
Dimensions, λs	196×379
Pixel size, cm	1.55×10^{-2}
Minimum aperture, cm	1.00×10^{-3}
Maximum aperture, cm	2.30×10^{-2}
$\langle b \rangle$, cm	1.0×10^{-2}
Standard deviation, cm	3.0×10^{-3}
Correlation length (λ), short axis, cm	0.07
Correlation length (λ), long axis, cm	0.08
RMS error, % of mean	2.2

The duration of each quasi steady time step must be short enough that entrapped-phase geometry does not change significantly from one time step to the next. We can verify that time steps are sufficiently short by comparing simulations using different values of Δt. If Δt is adequately small, the differences between these simulations will be insignificant. This is demonstrated for the simulations described in section 5.

4. A Physical Experiment

To test the computational model, we conducted a physical TCE-dissolution experiment in the transparent analog fracture fabricated by ZMG. We measure fracture aperture and TCE distribution within the fracture at resolutions (0.0155×0.0155 cm) that were much smaller than the correlation length (λ) of the aperture variability (0.07–0.08 cm) using light transmission techniques. TCE-distribution measurements acquired during the experiment could then be directly compared with the simulated evolution of TCE distribution under identical conditions (section 5).

4.1. Description of the Analog Fracture

ZMG fabricated the transparent analog fracture used in the current investigation by placing two 15.4×30.3 cm pieces of textured glass in contact and applying a confining pressure of 138 kPa (for fabrication details, see ZMG). We applied no-flux boundaries along the long edges of the fracture and flow manifolds along the short edges of the fracture. The inflow manifold provided uniformly distributed flow across the width of the fracture, while the outflow manifold consisted of four equally spaced ports pressed up against the fracture edge, through which equal flow was extracted at a constant rate. ZMG volumetrically measured the mean aperture for this fracture to be 0.010 cm. On the basis of their error analysis and the 0.1 g/L mixture of FD&C Blue #1 (Warner Jenkinson) used in the current investigation, the RMS error for individual aperture measurements was ~2.2% of the mean aperture (for aperture measurement and error analysis methods, see *Detwiler et al.* [1999]).

Table 1 summarizes the details of the aperture field measurements. The apertures are approximately normally distributed with a standard deviation of 3.0×10^{-3} cm (Figure 4). Semivariograms (γ) of the aperture field measured along the long and short axes of the fracture (Figure 5) indicate the aperture field is slightly anisotropic, with $\lambda \approx 0.07$ cm along the short axis and $\lambda \approx 0.08$ cm along the long axis. Figure 5 also shows negative correlation along both principal axes for sepa-
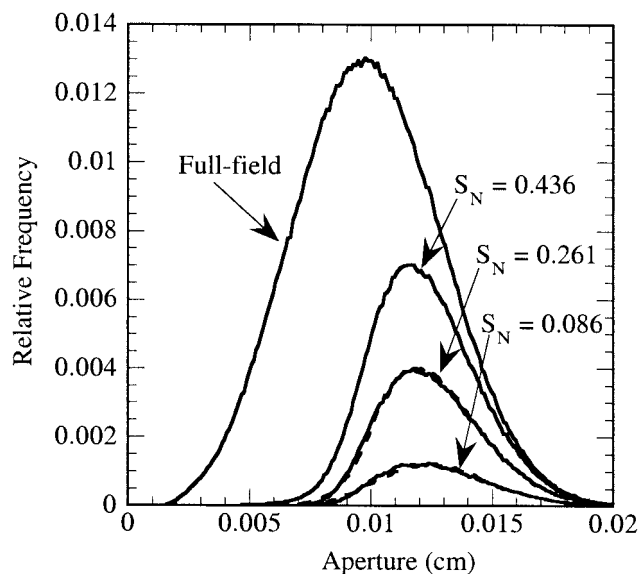

Figure 4. Distribution of fracture apertures in the experimental fracture. The experimental (solid lines) and simulated (dashed lines) distributions of NAPL-filled pixels at $S_N = 0.436$ (initial condition), 0.261, and 0.086 (final condition) are also shown.

rations ranging from ~0.1 to 0.2 cm. Absence of a level sill in both semivariograms indicates mild long-wavelength trends in the aperture field. These trends are due to long-wavelength (~5 cm) undulations in the individual pieces of glass, which are visible in gray scale images of the aperture field (see ZMG, Figure 2).

4.2. Experimental Procedure

A syringe pump pulled water from a constant-head container through the fracture and through the four independent outflow ports (i.e., each connected to a separate syringe). This
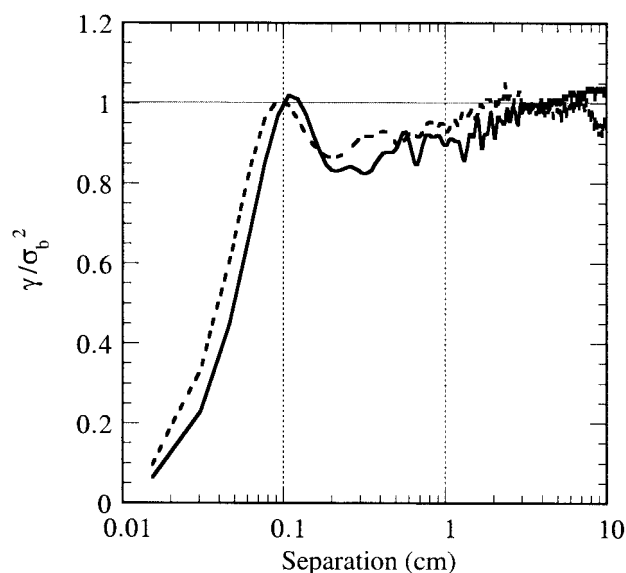

Figure 5. Semivariograms (γ) normalized by the variance (σ_b^2) of the fracture aperture field. The short-axis and long-axis correlation lengths (λ) are approximately 0.07 and 0.08 cm, respectively.

Table 2. Parameters Used in Dissolution Simulation

Property	Value	Reference
Molecular diffusion coefficient (D_M), cm^2/s at 21.5°C	9.3×10^{-6}	computed using method of *Wilke and Chang* [1955]
Density (ρ_{NAPL}) at 20°C, g/cm^3 at 20°C	1.465	*Kirk and Othmer* [1979]
Solubility (c_s), g/cm^3 at 21.5°C	$1.28\ 10^{-3}$g/L	*Imhoff* [1992]
Water-TCE-glass contact angle (α), degrees	76 ± 10	estimate from current study
Grid-spacing (Δx), cm	0.0155	N/A
Time step (Δt), hours	2.0	N/A
Flow rate, cm^3/s	3.605×10^{-3}	N/A

N/A, not applicable.

outflow configuration assured a relatively uniform initial NAPL distribution by eliminating phase blockage problems in the outflow manifold. A marriotte bottle provided a constant-head boundary condition at the inflow and maintained a slight vacuum on the water in the reservoir. The vacuum reduced the concentration of air dissolved in the water and prevented the formation of small air bubbles in the fracture and plumbing. To monitor flow rate, a balance recorded the mass of the marriotte bottle at 7.5-min intervals over the duration of the experiment (240 hours). A straight line fitted to a plot of inflow mass versus time gave a steady flow rate of $(3.605 \pm 0.001) \times 10^{-3}$ cm^3/s. The temperature in the room remained at 22.5 ± 0.5°C over the duration of the experiment.

The TCE properties that are relevant to dissolution are presented in Table 2. Because our ability to delineate the water and TCE in the fracture depends on differential light absorbance by the two fluids, we dyed the water with 0.25 g/L of FD&C Blue #1. This is in contrast to previously reported dissolution experiments involving NAPL visualization [e.g., *Powers et al.*, 1992; *Imhoff et al.*, 1996; *Kennedy and Lennox*, 1997; *Jia et al.*, 1999; ZMG], where the NAPL was dyed with oil-red-o. Because oil-red-o is not water soluble, its concentration in each NAPL blob increases as the blob shrinks due to dissolution. These variable concentrations can lead to complications in interpreting experimental data. Dyeing the water may reduce both the solubility and D_M of TCE in the aqueous phase; however, the effect should be both uniform (over the entire field) and constant (over the duration of the experiment).

Prior to initiating the experiment, we flushed the fracture with sulfuric acid (18 M, 38 g/L Nochromix) followed by a clean water flush. This cleaning process minimized variability of the contact angle (α) between TCE (nonwetting fluid) and water (wetting fluid) within the fracture. To initiate the experiment, we used the same experimental procedure as ZMG. We injected TCE into the water-saturated fracture at a flow rate of 0.2 mL/min until TCE reached each of the four outflow ports and then reestablished water flow through the fracture at the same flow rate. This flow rate was low enough to yield large, complex regions of residual entrapped NAPL and high enough to allow measurable dissolution over a reasonable time frame. The flowing water mobilized some TCE, leaving behind residual entrapped TCE at the initiation of the dissolution experiment (see ZMG, Figure 5, for representative TCE distributions before and after the mobilization step).

After mobilization ceased (~4 hours), we began measuring the evolution of TCE distribution within the fracture. The charge-coupled device (CCD) camera acquired sets of five images of the entire flow field every 15 min for the duration of the experiment. Essentially no change in the phase structure

occurred over the 40-s interval required to take the five images, so averaging each set of five images resulted in reduced signal noise and improved the accuracy of entrapped-TCE delineation. We calculated the phase distribution in each averaged image using an adaptive thresholding routine developed by *Nicholl and Glass* [1994] and improved upon by *Nicholl et al.* [2000]. This process resulted in binarized images in which pixels occupied by NAPL were assigned values of 1 and pixels occupied by flowing water were assigned values of 0. These binarized images provide a record of the evolution of TCE distribution within the fracture. Multiplying the binarized images with the measured aperture field yields measurements of S_N for each field, as well as dissolution rates that can be directly compared to computational simulations. Curvature of the NAPL-water interfaces between the fracture surfaces causes some light reflection and refraction, which results in some uncertainty in the exact location of interfaces. Varying the parameters used for the thresholding routine provided estimates of the sensitivity of the binarized images to a reasonable range of input parameters. On the basis of this analysis for the initial phase distribution field, the initial S_N of 0.436 has a possible range of ± 0.02. We expect the relative influence of these errors to be greater for small TCE blobs; however, the smallest blobs account for only a very small portion of the total volume of TCE.

4.3. Summary of Experimental Results

Figure 6 shows the TCE distribution in the fracture at the initiation of the dissolution experiment. Flow through the fracture was from left to right, and the solid and open regions represent entrapped TCE and water, respectively. A significant difference between our experiments and those of ZMG was that we simply dissolved the TCE without the additional mobilization induced with a surfactant flood. Thus the entrapped TCE blobs in our experiment were considerably more complex and representative of residual entrapped-phase structures under natural flow and dissolution conditions. The medium-sized continuous regions of water in the initial phase structure coincide with regions of slightly smaller aperture relative to the entire field. These regions of smaller aperture are the likely cause for the trends observed in the semivariograms.

Plate 1a is a composite of binarized phase distribution fields over the duration of the experiment. The color scale indicates the time at which a given location became water-filled; gray locations were initially water-filled, dark blue locations dissolved at early times, and red locations had not yet dissolved at the end of the experiment. The long strip of blue pixels aligned with the flow direction along the bottom half of the field indicates the early formation of a large-scale dissolution channel. A smaller dissolution channel began to form at early time

Figure 6. TCE distribution in the 15.4×30.3 cm fracture prior to initiation of the dissolution experiment and simulation. Solid areas represent entrapped TCE, and open areas represent water flowing from left to right.

near the top of the field as well, but its growth slowed when the main dissolution channel became well connected to three of the four outflow ports.

Some mobilization of TCE occurred during the experiment as small, localized movements of TCE that caused only redistribution within individual TCE blobs. These small movements are seen as discontinuities in the color scheme and are largely concentrated in the large red region at the upper right-hand side of the fracture (Plate 1a). These movements were likely due to small pressure changes when the syringe pump was emptied (~12-hour intervals) and periodic bubbling through the tube to the atmosphere in the marriotte bottle. However, the interplay of capillary forces within blobs as they shrink could also have created the redistribution. One would expect such capillary effects to be more important in large blobs, and, indeed, this is where the redistribution occurred.

5. Comparison of Dissolution Simulation to Experiment

To test the computational algorithm described in section 3, we simulated TCE dissolution in the measured aperture field using the experimentally measured initial TCE distribution as the initial condition. The properties of TCE and other parameters used in the simulation are summarized in Table 2. The grid-block size used in the simulation was 0.0155 cm (same as the pixel size used for experimental measurements of aperture and phase structure), which resulted in a 995×1952 grid. The relevant boundary conditions for the flow simulations were constant flux (equal to the experimentally measured flow rate) at each of the four outflow ports, constant pressure along the inflow edge, and no flux along the long edges of the fracture. For the transport simulations the boundary conditions were $C = 0$ at the inflow boundary, no flux across the long edges of the fracture, and $\partial C / \partial x = 0$ at the outflow ports. For the MIP

simulations of phase structure evolution, we used $\alpha = 76$ degrees and $\lambda = 0.07$ cm, which yielded reasonable agreement between simulated and experimentally observed blob shrinkage. The chosen value for α corresponds reasonably well with visual observations of receding TCE-water-glass contact angles. The dissolution simulation terminated at a value of $S_N = 0.086$, which corresponds to the last experimental measurement.

Plate 1b shows the phase structure evolution during the dissolution simulation corresponding to the experimental composite image (Plate 1a). Comparing Plates 1a and 1b demonstrates that the simulation closely reproduces the large-scale evolution of the phase structure over the entire field. Discrepancies between Plates 1a and 1b are mostly concentrated near the lower edge of the fracture, with relatively minor local discrepancies at other locations. These results demonstrate the ability of the dissolution model, which couples mass transfer and interface movement, to track the evolution of the entrapped-TCE structure at the scale of the fracture. Plates 1c and 1d show the dissolution order in a single blob for the experiment and simulation, respectively, and Plate 1e shows the simulated dissolution of the same blob using a standard invasion percolation (SIP) model (i.e., calculation of the interface curvature excludes the contribution of in-plane curvature). The MIP simulation more closely represents the general behavior of the shrinking blob than the SIP simulation. Most notably, as the blob breaks up, the experiment and the MIP algorithm both produce daughter blobs that connect several regions of large aperture through regions of smaller aperture. Because the SIP algorithm will always fill the smallest aperture along an interface first, it results in smaller and disconnected blobs as the original blob dissolves and breaks up.

Plate 2 shows simulated concentration fields at three different TCE saturations ($S_N = 0.436$, 0.261, and 0.086). Several features observed in these concentration fields highlight the
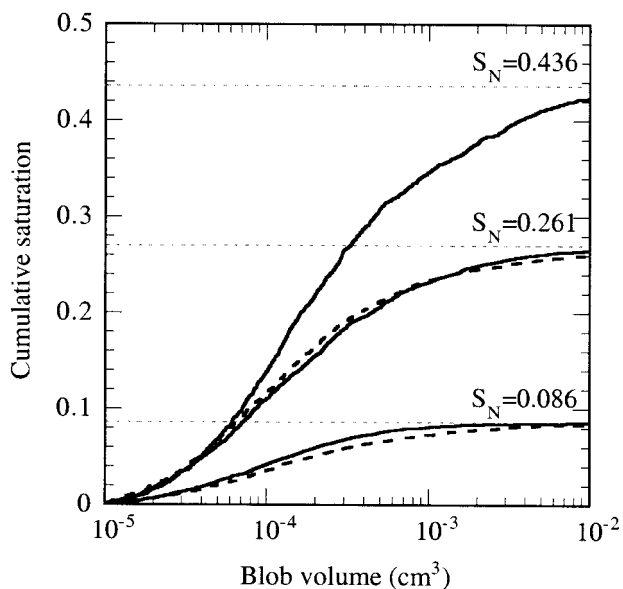
Figure 7. Cumulative saturation distribution of the TCE-blob volumes for the experiment (solid lines) and the simulation (dashed lines) at $S_N = 0.436$, 0.261, and 0.086.

Figure 8. TCE saturation (S_N) normalized by the initial saturation (S_{Ni}) plotted against time for the experiment and simulation.

influence of small-scale hydrodynamics on dissolution, as suggested earlier by *Glass and Nicholl* [1995]. (1) Plate 2a demonstrates the channeling of clean water entering the fracture, which is influenced by the structure of the entrapped phase within the fracture. Such channeling eventually leads to pronounced dissolution channels (Plate 2c) along which TCE dissolves rapidly, while leaving behind substantial mass outside of these channels. (2) Examination of Plates 1a and 1b reveals that dense clusters and large, tortuous TCE blobs dissolve at a slower rate than smaller blobs. The concentration fields in Plate 2 demonstrate that flow is largely diverted around these large blobs and significant mass transfer occurs only from a small portion of their perimeter. (3) Regions of high mass transfer (i.e., large aqueous-phase-TCE concentration gradients) do not necessarily coincide with locations of rapid interface movement. Examining the evolution in time of the TCE phase in the boxed region of Plates 2b and 2c clarifies this point. The concentration gradients surrounding this blob are highest at the upstream end (see Plate 2b). However, comparing Plates 2b and 2c, it is evident that the TCE has withdrawn from the downstream portion of the boxed region, while the upstream end shows little change in the TCE-phase occupancy. As the blob volume reduces due to dissolution, the remaining TCE continues to recede into the upstream end, where local apertures are larger. This vividly illustrates the importance of coupling mass transfer and capillary physics for simulating dissolution of an entrapped phase in variable-aperture fractures.

Histograms of TCE-filled apertures in Figure 4 for $S_N = 0.436$, 0.261, and 0.086 show excellent agreement between the experiment and the simulation. Because TCE is the nonwetting fluid, the initial ($S_N = 0.436$) median TCE-filled aperture is ~15% larger than the median of the entire field. As TCE dissolves, it more frequently leaves the smaller apertures, causing the distribution to become slightly skewed toward the larger apertures. Figure 7 shows cumulative saturation distribution of TCE-blob volumes for the experiment and simulation for $S_N = 0.436$, 0.261, and 0.086. Owing to the previ-
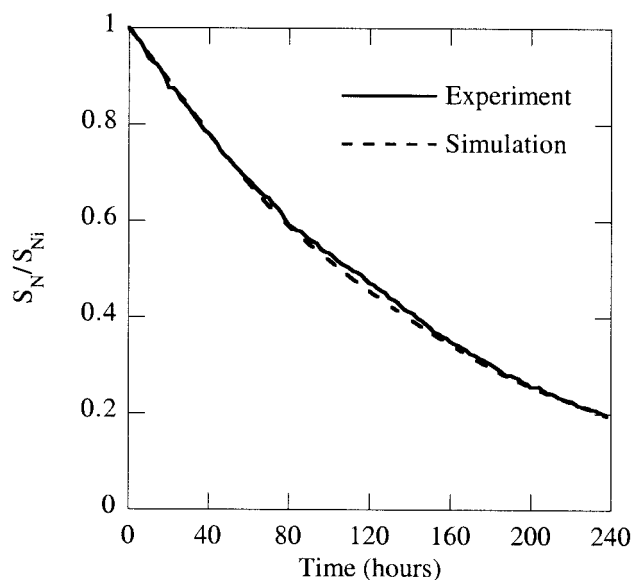
ously mentioned difficulties with detecting small NAPL blobs with the experimental system, we removed all NAPL blobs that were less than 1×10^{-5} cm^3 from the simulated and experimental fields. This cutoff volume corresponds to blobs that occupied less than about five pixels; removing these blobs from each field resulted in less than a 0.1% reduction in total mass. Note that the measured blob volumes for this experiment range over more than 3 orders of magnitude, in contrast to blob volume measurements in a homogeneous porous media [*Mayer and Miller*, 1992], which ranged over ~2 orders of magnitude. As with previous measurements in porous media, the experimentally measured blob-volume distributions are approximately lognormally distributed at each saturation. The most significant change in the distributions is that as S_N decreases, the number of large blobs also decreases. The experiment and simulation exhibit good agreement over the range of S_N and over the range of blob volumes.

Considering the dissolution behavior at the scale of the fracture, Figure 8 shows the experimental and simulated time variation of total TCE saturation (S_N) normalized with respect to the initial value ($S_{Ni} = 0.436$). The simulation accurately reproduces the time variation of the NAPL saturation over the duration of the experiment ($S_N = 0.436$–0.086), despite the local, small-scale discrepancies mentioned previously. It is also interesting to note that for both the experiment and the simulation, the decay of S_N with time can be modeled well by an exponential

$$S_N/S_{Ni} = \exp\left[-Kt(C_s - C)/\rho\right], \qquad (24)$$

where K is a bulk mass transfer coefficient and C is some fracture-scale average concentration (e.g., influent concentration, C_o). Fitting (24) to a plot of the evolution of S_N with time (Figure 8) yields estimates of $K = (6.49 \pm 0.02) \times 10^{-3}$ hour^{-1} and $(6.64 \pm 0.02) \times 10^{-3}$ hour^{-1} for the experiment and simulation, respectively. The fact that a single parameter describes the dissolution rate in this fracture, despite the significant fingering of the entrapped TCE structure caused by dissolution, is a feature that merits further study. A modified
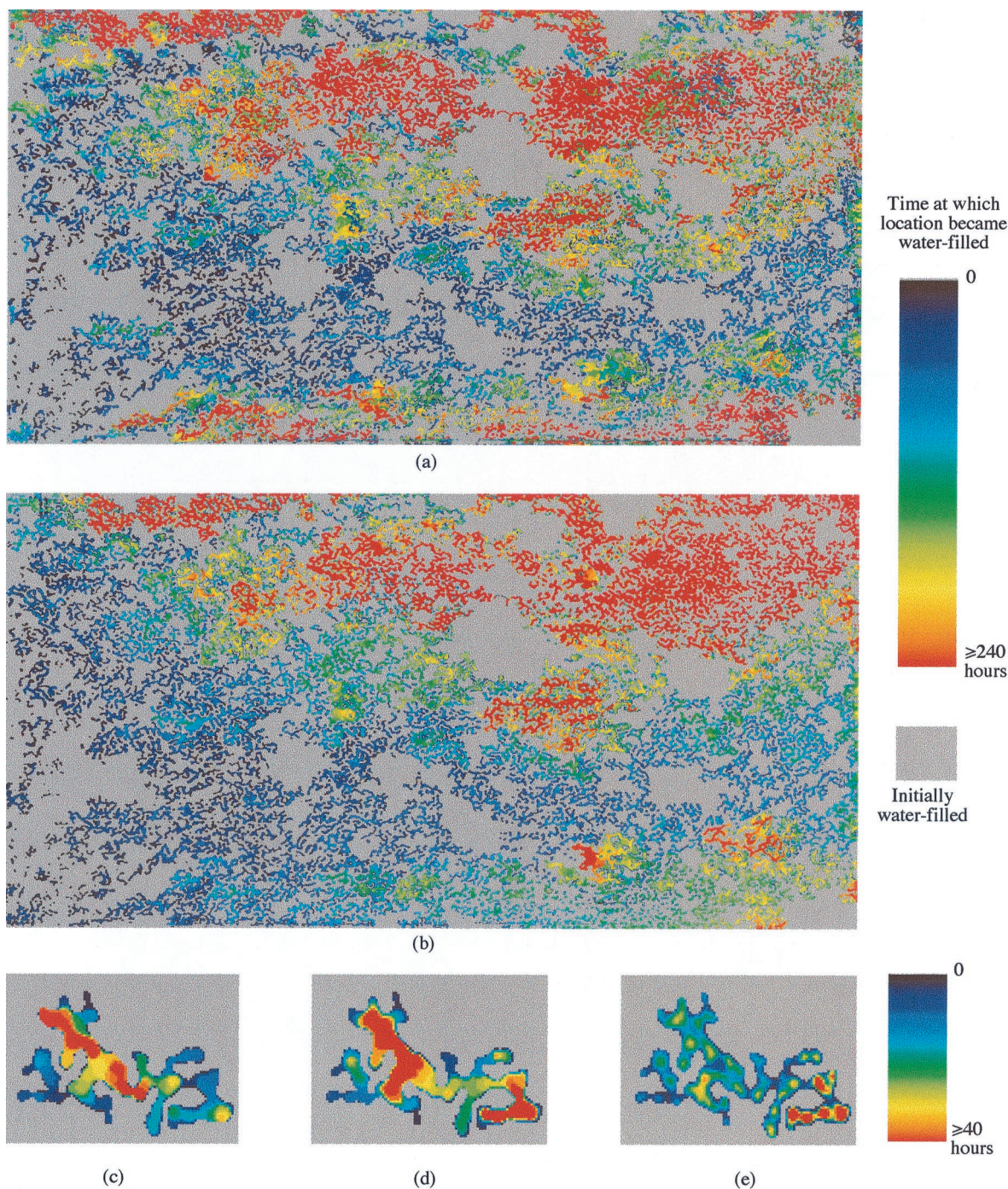
Plate 1. Composite images of TCE distribution with time for the (a) experiment and (b) simulation; flow through the fracture was from left to right. Evolution of a single TCE blob (located approximately one fifth of the fracture from the left-hand side and midway between the top and bottom) from (c) the experiment, (d) the MIP-based simulation, and (e) a standard invasion-percolation-based simulation (i.e., P_c calculated using only r_1).

dissolution simulation that utilized an open manifold (i.e., uniform head) boundary condition at the outflow confirmed that the dissolution fingering observed in the experiment was not an artifact of the outflow port configuration but a result of the complex initial TCE geometry and the feedback between dissolution and local permeabilities that has been observed to cause dissolution fingering in porous media [*Imhoff et al.*, 1996]. The only significant deviation between the modified simulation and the experiment occurred after the main dissolution channel became well connected to the outflow manifold, at which time the experimental configuration caused the main dissolution channel to broaden at the outflow end of the fracture. The ability of a simple mass transfer model (24) to describe the evolution of S_N during the experiment is encouraging in the context of developing effective mass transfer coefficients for entrapped NAPL dissolution in variable-
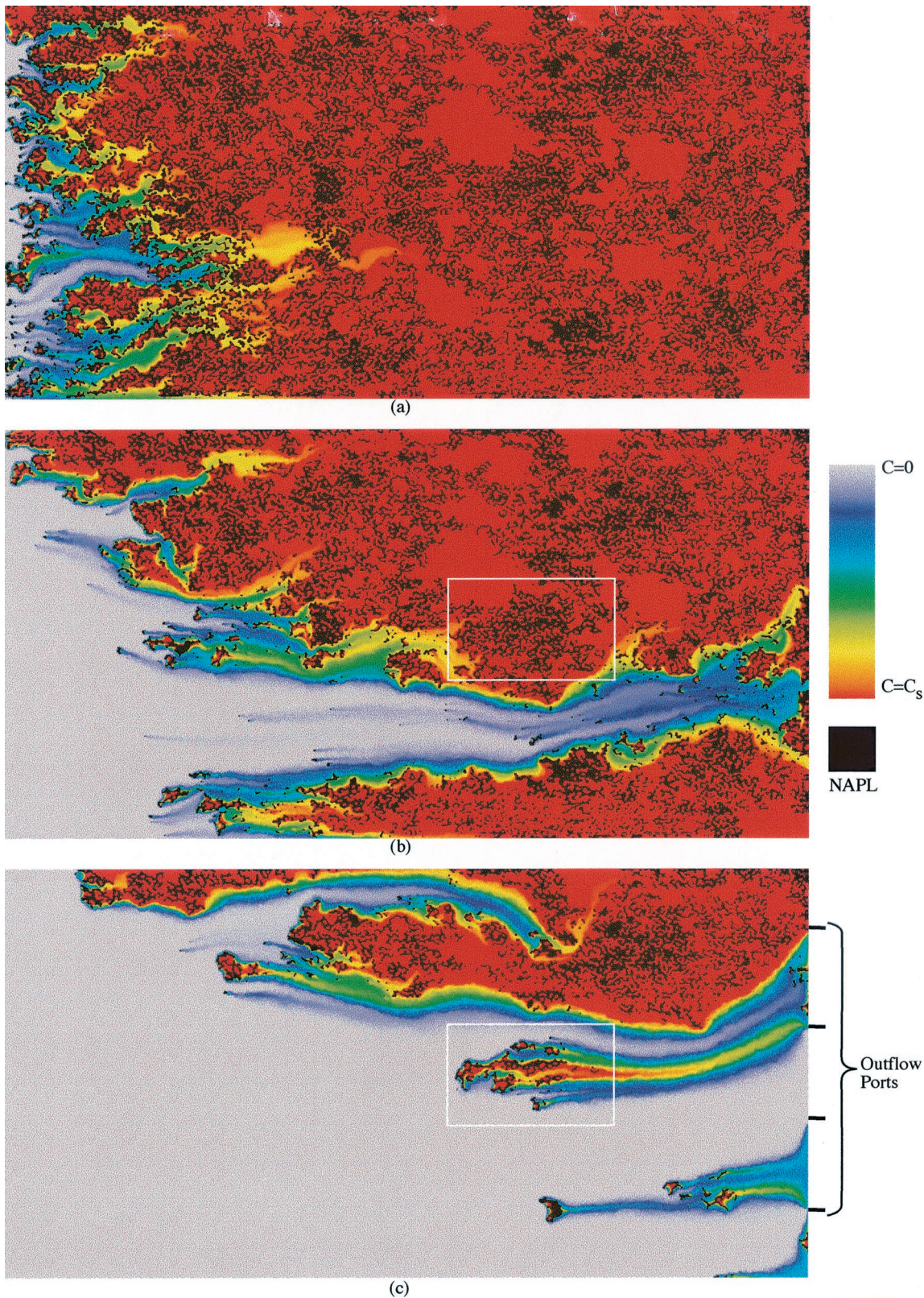
Plate 2. Concentration fields from the dissolution simulation for (a) $S_N = 0.436$ (initial saturation), (b) $S_N = 0.261$, and (c) $S_N = 0.086$. Removal of TCE from the boxed region in Plates 2b and 2c illustrates the importance of coupling mass transfer and capillary physics for simulating dissolution of an entrapped phase in variable-aperture fractures; mass transfer rates are highest in the left-hand portion of the boxed region, yet capillary forces cause TCE to recede more quickly from the right-hand portion of the boxed region.

aperture fractures. However, the results of the modified simulation suggest that as dissolution fingers become hydraulically well connected to the outflow end of the fracture, bypassing of flow past significant portions of the fracture may cause dissolution rates to slow and (24) to break down.

We emphasize that our simulation used only measured physical parameters and no empirical relationships. It is useful then to consider the sensitivity of dissolution simulations to errors in estimates of the physical parameters, including the molecular diffusion coefficient of TCE dissolved in water (D_m), density (ρ), and contact angle (α). In addition, the robustness of the computational algorithm must be confirmed, in particular, the sensitivity of simulations to values of $\mathbf{D}_{\text{eff}}$, Δx, and Δt. Sensitivity studies for D_m and α (and any other factor which can modify the interface area A in equation (21)) revealed that an increase in D_m or A is accompanied by a decrease in the computed concentration gradient ($\nabla C \cdot \mathbf{n}$) at the interface, such that a 10% increase in D_m or A leads to only a 1.3% increase in the mass transfer rate at an interface. Thus errors in estimates of D_m or other properties controlling A will only result in relatively small deviations in simulated mass transfer rates. However, mass transfer rates are directly proportional to the TCE density ρ. Fortunately, it is easier to obtain accurate measurements of ρ than either D_m or A, so errors in ρ should not be a source of significant errors in simulated mass transfer rates.

To test the sensitivity of our simulation to the value of $\mathbf{D}_{\text{eff}}$, we replaced $\mathbf{D}_{\text{eff}} = D_m$ (used in the previously discussed simulations) with $\mathbf{D}_{\text{eff}} = D_m(1 + Pe^2/210)$ and repeated the dissolution simulation. It should be noted that the size of a grid block (0.0155 cm) is close to the mean aperture (0.010 cm). Thus the use of the asymptotic Taylor dispersion coefficient, which requires a distance of $0.4Peb$ to develop, will significantly overestimate the actual magnitude of Taylor dispersion effects. We are using this large value to test the sensitivity of our simulation results. Development of a consistent representation for the grid-block-scale effective Taylor dispersion coefficient is a problem that merits further study. In the initial TCE distribution field, values of Pe ranged from 0 to 331, which results in local values of $\mathbf{D}_{\text{eff}}$ ranging from D_m to $525D_m$. Despite this wide range of local dispersion coefficients, simulated dissolution rates are not substantially different from those obtained using $\mathbf{D}_{\text{eff}} = D_m$ (Figure 9). The concentration fields shown in Plate 2 are helpful in understanding this somewhat surprising result. Concentration gradients in the flow direction are uniformly small, and thus, despite the large values of $\mathbf{D}_{\text{eff}}$, the dispersion in the flow direction is insignificant. Conversely, transverse dispersion, which controls mass transfer rates at NAPL-water interfaces, is unaffected by the alternative form for $\mathbf{D}_{\text{eff}}$. These results suggest that using $\mathbf{D}_{\text{eff}} = D_m$ is reasonable in this depth-averaged model of dissolution.

We also examined the influence of numerical dispersion on the simulated dissolution rate. As we discussed in section 3, the upwind finite difference scheme used to discretize the advective term in (19) is susceptible to numerical dispersion in regions of high grid-Pe ($\mathbf{v}\Delta x/2D_m$) and steep concentration gradients. Because the numerical dispersion coefficient is proportional to $\nu\Delta x$, we expect that it will have less of an influence on mass transfer rates than using $\mathbf{D}_{\text{eff}} = D_m(1 + Pe^2/210)$. To evaluate the influence of numerical dispersion on the dissolution simulation, we refined the grid (i.e., reduced the grid-Pe) by a factor of 2 and repeated the simulation using identical
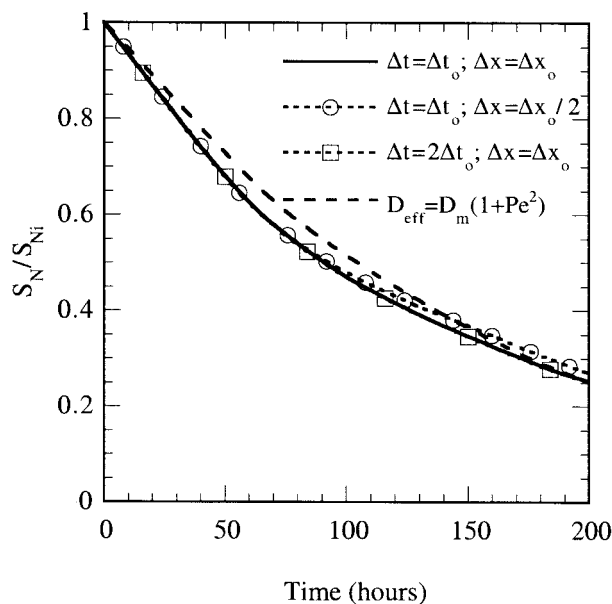

Figure 9. TCE saturation (S_N) normalized by the initial saturation (S_{Ni}) plotted against time for simulations using different values of Δt and Δx. The simulation compared with the experiment in Figure 8 used values of $\Delta t_o = 2$ hours and $\Delta x_o = 0.0155$ cm. The close agreement between the original simulations and simulations with $\Delta t = 2\Delta t_o$ and $\Delta x = \Delta x_o/2$ demonstrates that the values of Δt and Δx used in the original simulation are adequately small. Also shown is a simulation with the local effective dispersion coefficient ($\mathbf{D}_{\text{eff}}$) represented by the Taylor dispersion coefficient between parallel plates rather than D_m used in the other simulations. Though we expect this to be a significant overestimation of $\mathbf{D}_{\text{eff}}$, the plot is in close agreement with the other simulations.

parameters. We reduced the size of the coarse-grid domain to 795×1952 by removing a strip of 100 grid blocks along the no-flux edges of the domain; this slight reduction in size was necessary for the refined-grid simulation (1590×3904) to run efficiently on the Sun Enterprise 250 (2 Gb RAM) workstation used for these simulations. Despite the fact that there are local regions of high grid-Pe in the coarse-grid field, the fine-grid simulation demonstrated excellent agreement with the coarse-grid simulation on the same domain (Figure 9). We thus conclude that our fracture-scale estimates of dissolution rates are not biased by numerical dispersion.

Finally, we examined the influence of Δt on the simulation by increasing Δt by a factor of 2 to $\Delta t = 4$ hours. Figure 9 compares plots of S_N against time for $\Delta t = 2$ and 4 hours and suggests that $\Delta t = 2$ hours was an adequately short time step for this fracture, initial TCE distribution, and flow rate. These results also suggest that our approach for tracking mass in NAPL blobs that are smaller than one grid block (described in section 3) does not have a significant influence on our results.

6. Concluding Remarks

We have presented a depth-averaged computational model for simulating dissolution of an entrapped NAPL in variable-aperture fractures that couples flow, dissolved NAPL transport, and interphase mass transfer with the capillary-defined interface movement. Flow is modeled using the Reynolds equation, and transport of the dissolved NAPL is modeled

using the corresponding depth-averaged solute transport equation; both of these models assume an impermeable rock matrix. By directly solving for the depth-averaged velocity field around each entrapped NAPL blob, and assuming that the dissolved NAPL is at equilibrium at NAPL-water interfaces, the model does not require empirical relationships to describe local mass transfer rates. We have shown that a quasi steady state approximation is appropriate in the case of a NAPL for which the solubility limit in water is very small compared with its density. On the basis of this approximation, a sequence of quasi steady flow and concentration fields corresponding to the evolving NAPL phase structure can be used to compute dissolution rates. Because entrapped NAPL blobs may have in-plane dimensions that are many times the aperture correlation length, it is critical to incorporate capillary physics into the computation of the interface movements that modify the flow field as the phase structure evolves. We are unaware of any previous model formulations that establish such a coupling. This depth-averaged model offers a computationally tractable framework for developing constitutive relationships between mass transfer rates and parameters characterizing the NAPL phase structure, aperture variability, and the mean flow rates. Such constitutive relationships may then be used to represent single fractures within large-scale network models.

To test the computational model, we compared a dissolution simulation based on the depth-averaged model with a TCE dissolution experiment in an analog fracture. Using light transmission techniques, we measured the fracture aperture and the evolution of the TCE distribution over the 240-hour duration of the experiment. The high resolution of these measurements (0.0155×0.0155 cm) resulted in approximately five measurements per correlation length over the entire 15.4×30.3 cm flow field. The resulting 995×1952 computational grid corresponded with the measured fields; to our knowledge, these are the first computations of entrapped-phase dissolution in grids with $O(10^6)$ nodes. The results of the computational simulation agreed closely with the experiment, suggesting that despite a number of simplifications implicit in depth averaging the three-dimensional governing equations, this model can be used as a tool for developing a general understanding of the process of dissolution from single variable-aperture fractures.

The excellent agreement between simulation and experiment is in part due to the careful design of the experiment to avoid some of the known limitations of the depth-averaged approach. It is important to consider these limitations in any attempt to use this model as a predictive tool. The validity of the Reynolds equation depends on the values of $\langle b \rangle / \lambda$ and $\sigma_b / \langle b \rangle$. *Zimmerman and Bodvarsson* [1996] suggested that the effective transmissivity of a rough-walled fracture is adequately quantified using the Reynolds equation, if the value of $\langle b \rangle / \lambda$ is smaller than about 0.05. In our experimental fracture, $\langle b \rangle / \lambda$ is 0.12 and $\sigma_b / \langle b \rangle = 0.3$; in a fracture with similar values of these parameters, *Nicholl et al.* [1999] observed that the Reynolds equation overestimates the effective transmissivity by about 32%. However, in our simulation, we minimized local errors in the simulated flow field by specifying the experimentally measured constant flux through the fracture. In addition, the depth-averaged approximation of the transport equation used here does not incorporate the influence of Taylor dispersion. Our sensitivity analysis demonstrated that using local values of $\mathbf{D}_{eff}$ that overestimate the influence of Taylor dispersion does not result in significant changes in dissolution rates. However, developing a theoretical expression for local values

of $\mathbf{D}_{eff}$ to be used in depth-averaged transport simulators is an area that merits further study.

An important motivation for developing constitutive relations for the dissolution process arises from the need to represent the effective behavior of variable-aperture fractures in large-scale discrete fracture network models. In these large-scale models it is infeasible to represent detailed aperture variability within single fractures. Our experimental and simulation results indicate an exponential decay in the NAPL saturation (S_N) with time, suggesting the validity of the simple linear mass transfer model (24) for describing fracture-scale behavior. It is especially surprising that the fracture-scale mass transfer coefficient is essentially constant during the dissolution process, despite the significant changes in the entrapped NAPL phase structure. This is a feature that merits further study. The fracture-scale mass transfer coefficient is presumably related to Pe, the initial entrapped phase structure (which is in turn influenced by the combination of capillary, gravity, and viscous forces with invasion history), and other parameters characterizing aperture variability. Detailed parametric studies covering a wide range of conditions will further clarify the nature of this relationship. Such parametric studies will be valuable in leading to meaningful representations of single fractures in large-scale fracture network models. The depth-averaged model presented here can also be extended to incorporate matrix diffusion and other mechanisms of exchange of water and solute between fractures and the adjacent rock matrix, leading ultimately to physically consistent models of NAPL dissolution in fractured rock masses.

References

Adler, P. M., and J.-F. Thovert, *Fractures and Fracture Networks*, Kluwer Acad., Norwell, Mass., 1999.

Brown, S. R., Fluid flow through rock joints: The effect of surface roughness, *J. Geophys. Res.*, *92*(B2), 1337–1347, 1987.

Conrad, S. H., J. L. Wilson, W. R. Mason, and W. J. Peplinski, Visualization of residual organic liquid trapped in aquifers, *Water Resour. Res.*, *28*, 467–478, 1992.

Detwiler, R. L., S. E. Pringle, and R. J. Glass, Measurement of fracture aperture fields using transmitted light: An evaluation of measurement errors and their influence on simulations of flow and transport through a single fracture, *Water Resour. Res.*, *35*, 2605–2617, 1999.

Detwiler, R. L., H. Rajaram, and R. J. Glass, Solute transport in variable-aperture fractures: An investigation of the relative importance of Taylor dispersion and macrodispersion, *Water Resour. Res.*, *36*, 1611–1625, 2000.

Dillard, L. A., and M. J. Blunt, Development of a pore network simulation model to study nonaqueous phase liquid dissolution, *Water Resour. Res.*, *36*, 439–454, 2000.

Gelhar, L. W., Application of stochastic models to solute transport in fractured rocks, report, Swed. Nucl. Fuel and Waste Manage. Co., Stockholm, Sweden, 1987.

Glass, R. J., and M. J. Nicholl, Quantitative visualization of entrapped phase dissolution in a horizontal flowing fracture, *Geophys. Res. Lett.*, *22*, 1413–1416, 1995.

Glass, R. J., M. J. Nicholl, and L. Yarrington, A modified invasion percolation model for low-capillary number immiscible displacements in horizontal rough-walled fractures: Influence of local in-plane curvature, *Water Resour. Res.*, *34*, 3215–3234, 1998.

Glass, R. J., M. J. Nicholl, and L. Yarrington, Correction to "A modified invasion percolation model for low-capillary number immiscible displacements in horizontal rough-walled fractures: Influence of local in-plane curvature," *Water Resour. Res.*, *36*, 1991, 2000.

Imhoff, P. T., Dissolution of a nonaqueous phase liquid in saturated porous media, Ph.D. dissertation, Princeton Univ., Princeton, N. J., 1992.

Imhoff, P. T., P. R. Jaffé, and G. F. Pinder, An experimental study of complete dissolution of a nonaqueous phase liquid in saturated porous media, *Water Resour. Res.*, *30*, 307–320, 1994.

Imhoff, P. T., G. P. Thyrum, and C. T. Miller, Dissolution fingering during the solubilization of nonaqueous phase liquids in saturated porous media, 2, Experimental observations, *Water Resour. Res.*, *32*, 1929–1942, 1996.

Jia, C., K. Shing, and Y. C. Yortsos, Visualization and simulation of non-aqueous phase liquids solubilization in pore networks, *J. Contam. Hydrol.*, *35*, 363–387, 1999.

Kennedy, C. A., and W. C. Lennox, A pore-scale investigation of mass transport from dissolving DNAPL droplets, *J. Contam. Hydrol.*, *24*, 221–246, 1997.

Kirk, T. E., and D. F. Othmer, *Encyclopedia of Chemical Technology*, 3rd ed., vol. 5, Wiley-Interscience, New York, 1979.

Larson, R. G., L. E. Scriven, and H. T. Davis, Percolation theory of two phase flow in porous media, *Chem. Eng. Sci.*, *36*, 57–73, 1981.

Leal, L. G., *Laminar Flow and Convective Transport Processes: Scaling Principles and Asymptotic Analysis*, Butterworth-Heinemann, Woburn, Mass., 1992.

Mackay, D. M., and J. A. Cherry, Groundwater contamination: Pump-and-treat remediation, *Environ. Sci. Technol.*, *23*, 630–636, 1989.

Mayer, A. S., and C. T. Miller, The influence of porous medium characteristics and measurement scale on pore-scale distributions of residual nonaqueous-phase liquids, *J. Contam. Hydrol.*, *11*, 189–213, 1992.

Miller, C. T., M. M. Poirier-McNeill, and A. S. Mayer, Dissolution of trapped nonaqueous phase liquids: Mass transfer characteristics, *Water Resour. Res.*, *26*, 2783–2796, 1990.

Moreno, L., Y. W. Tsang, C. F. Tsang, F. V. Hale, and I. Neretnieks, Flow and tracer transport in a single fracture: A stochastic model and its relation to some field observations, *Water Resour. Res.*, *24*, 2033–2048, 1988.

Nicholl, M. J., and R. J. Glass, Wetting phase permeability in a partially saturated horizontal fracture, paper presented at the Fifth Annual International Conference on High Level Radioactive Waste Management, Am. Nucl. Soc., Las Vegas, Nev., May 22–26, 1994.

Nicholl, M. J., H. Rajaram, R. J. Glass, and R. L. Detwiler, Saturated flow in a single fracture: Evaluation of the Reynolds equation in measured aperture fields, *Water Resour. Res.*, *35*, 3361–3373, 1999.

Nicholl, M. J., H. Rajaram, and R. J. Glass, Factors controlling satiated relative permeability in a partially saturated horizontal fracture, *Geophys. Res. Lett.*, *27*, 393–396, 2000.

Ortoleva, P., E. Merino, C. Moore, and J. Chadam, Geochemical self organization, 1, Reaction-transport feedbacks and modeling approach, *Am. J. Sci.*, *287*, 979–1007, 1987.

Powers, S. E., L. M. Abriola, and W. J. Weber, An experimental investigation of nonaqueous phase liquid dissolution in saturated subsurface systems: Steady state mass transfer rates, *Water Resour. Res.*, *28*, 2691–2705, 1992.

Powers, S. E., L. M. Abriola, and W. J. Weber, An experimental investigation of nonaqueous phase liquid dissolution in saturated subsurface systems: Transient mass transfer rates, *Water Resour. Res.*, *30*, 321–332, 1994.

Ruge, J. W., and K. Stüben, Algebraic multigrid, in *Multigrid Methods*, edited by S. F. McCormick, pp. 73–130, Soc. for Ind. and Appl. Math., Philadelphia, Pa., 1987.

Schwartz, F. W., J. A. Cherry, and J. R. Roberts, A case study of a chemical spill: Polychlorinated biphenyls (PCBs), 2, Hydrogeological conditions and contaminant migration, *Water Resour. Res.*, *18*, 535–545, 1982.

Thompson, M. E., Numerical simulation of solute transport in rough fractures, *J. Geophys. Res.*, *96*(B3), 4157–4166, 1991.

Tsang, Y. W., and P. A. Witherspoon, Hydromechanical behavior of a deformable rock fracture, *J. Geophys. Res.*, *86*(B10), 9287–9298, 1981.

Wilke, C. R., and P. Chang, Correlation of diffusion coefficients in dilute solutions, *AIChE J.*, *1*, 264–270, 1955.

Yeo, I. W., M. H. DeFreitas, and R. W. Zimmerman, Effect of shear displacement on the aperture and permeability of a rock fracture, *Int. J. Rock Mech. Min. Sci.*, *35*, 1051–1070, 1998.

Zhong, L., A. Mayer, and R. J. Glass, Visualization of surfactant-enhanced nonaqueous phase liquid mobilization and solubilization in a two-dimensional micromodel, *Water Resour. Res.*, *37*, 523–537, 2001.

Zhou, D., L. A. Dillard, and M. J. Blunt, A physically based model of dissolution of nonaqueous phase liquids in the saturated zone, *Transp. Porous Media*, *39*, 227–255, 2000.

Zimmerman, R. W., and G. S. Bodvarsson, Hydraulic conductivity of rock fractures, *Transp. Porous Media*, *23*, 1–30, 1996.

———————————
R. L. Detwiler, Lawrence Livermore National Laboratory, P.O. Box 808, L-206, Livermore, CA 94551, USA. (detwiler1@llnl.gov)

R. J. Glass, Flow Visualization and Processes Laboratory, Sandia National Laboratories, Albuquerque, NM 87123, USA. (rjglass@sandia.gov)

H. Rajaram, Department of Civil, Environmental, and Architectural Engineering, University of Colorado, Boulder, CO 80309-0428, USA. (hari@thaneer.colorado.edu)